Original article

# Enhancing the Spatial Resolution of the AMSR2 C-Band Radiometer Channels for Monitoring the Arctic Seas Using the 36.5 Ghz Measurement Channels

E. V. Zabolotskikh <sup>1, ⊠</sup>, B. Chapron <sup>2</sup>

<sup>1</sup> Russian State Hydrometeorological University, Saint Petersburg, Russian Federation <sup>2</sup> Institut Français de Recherche pour l'Exploitation de la Mer, Ifremer, Plouzané, France liza@rshu.ru

#### Abstract

Purpose. The purpose of the work is to study the potential for improving the spatial resolution of the Advanced Microwave Scanning Radiometer 2 (AMSR2) on C-band channels using the measurements at 36.5 GHz frequency to analyze the underlying surface parameters of the Arctic seas.

Methods and Results. The results of numerical modeling of the brightness temperature (Tb) of microwave radiation from the sea ice-ocean-atmosphere system under conditions of the non-scattering Arctic atmosphere, as well as the calculations of Tb for the atmospheric and oceanic parameters based on the ERA5 reanalysis data were used. The values of sea ice effective emission coefficients previously calculated for the entire Arctic region were applied in calculations. The Tb sensitivity to atmospheric radiation, surface temperature and underlying surface emission coefficients at the 6.9 and 36.5 GHz measurement channels at the horizontal and vertical polarizations, and also variability of the above parameters in the Arctic were assessed. Depending on the surface type and based on the modeling results, proposed are the formulas for calculating the Tb fields at the 6.9 GHz frequency at the enhanced spatial resolution, in which Tb at the 6.9 GHz frequency of the original resolution and Tb at the 36.5 GHz frequency of the Level 1R satellite product were used.

Conclusions. The developed approach expands the possibilities of using the AMSR2 data for a detailed study of the parameters of Arctic seas partially or completely covered with first-year ice of various types and concentration. For the areas of continuous multi-year consolidate ice, application of the described method to improving the spatial resolution of measurements at 6.9 GHz, especially in vertical polarization, seems impossible. The errors and applicability of the above approach are conditioned by the variability of atmospheric water content parameters in a low spatial resolution pixel of measurements at the 6.9 GHz frequency.

**Keywords:** AMSR2, brightness temperature, spatial resolution, Arctic, sea ice-ocean-atmosphere system, physical modeling, sea ice

**Acknowledgments:** The study was carried out within the framework of state assignment of the Ministry of Science and Higher Education of RF No. FSZU-2025-0005 "The Arctic Sea ice-ocean-atmosphere system: Development of satellite methods and models".

**For citation:** Zabolotskikh, E.V. and Chapron, B., 2025. Enhancing the Spatial Resolution of the AMSR2 C-Band Radiometer Channels for Monitoring the Arctic Seas Using the 36.5 Ghz Measurement Channels. *Physical Oceanography*, 32(5), pp. 703-722.

© 2025, E. V. Zabolotskikh, B. Chapron

© 2025, Physical Oceanography

## Introduction

Satellite passive microwave remote sensing is widely used for global monitoring of atmospheric and underlying surface parameters due to its all-weather capability and independence from solar illumination. The ability to penetrate clouds is a key

ISSN 1573-160X PHYSICAL OCEANOGRAPHY VOL. 32 ISS. 5 (2025)





advantage of microwave instruments, enabling regular and continuous mapping of various parameters. Typically, microwave radiometers are multi-frequency and multi-polarization instruments, registering microwave radiation from the atmosphere and the Earth's surface at different frequencies and polarizations. These measurements are used for obtaining global data on atmospheric water vapor [1], cloud liquid water [2], sea surface temperature [3], sea ice concentration [4], snow water equivalent [5] and soil moisture [6].

However, microwave radiometer measurements have lower spatial resolution compared to infrared and optical instruments [7–9]. Furthermore, different channels within the same instrument have different spatial resolutions [10], resulting in multichannel algorithms yielding outputs with the lowest resolution among the channels used [11]. The low spatial resolution hinders the application of satellite microwave radiometer data for regional studies relating phenomena and objects smaller than the measurement resolution. While many atmospheric parameters over oceans are retrieved with high accuracy, estimations near coastlines are impossible due to land contamination of surface radiation, leading to masked areas in standard satellite products. Consequently, valuable information is lost, particularly in forecast models. Some of the late research studies focused on improving spatial resolution to enhance the accuracy of weather forecasts and climate models [12, 13].

The low spatial resolution of radiometric data is a result of signal averaging within the large antenna patterns of radiometric antennas and noise in the receivers. Several approaches have been developed to improve the spatial resolution. They may be categorized into the three main groups: data fusion algorithms, which incorporate higher-resolution data; antenna pattern inversion algorithms; and deep learning methods. Data fusion methods use ancillary information from optical observations [14] or higher-frequency channel measurements [15] with enhanced resolution. Antenna pattern inversion algorithms analyze data from overlapping pattern areas [9, 16]. Machine learning methods, particularly those using convolutional neural networks, employ the algorithms trained on ancillary high-resolution data [17, 18].

In [19], a method for enhancing the spatial resolution of optical images, known as Smoothing Filter-based Intensity Modulation (SFIM), was proposed, based on a simplified model of signal reflection from the Earth's surface. The method utilizes the ratio between the original high-resolution image signal and its smoothed signal, obtained via a low-pass filter, to modulate a lower spatial resolution image without changing its spectral properties or contrast. This approach effectively improves the spatial resolution of images. For optical instruments, spatial and spectral resolutions are often conflicting parameters: at a given signal-to-noise ratio, increasing spectral resolution (narrower spectral band) typically reduces spatial resolution.

The digital number (DN) of an optical image in a spectral reflective band  $\lambda$  primarily depends on the solar radiation incident on the Earth's surface (illuminance  $E(\lambda)$ ) and the spectral reflectance of the surface  $r(\lambda)$ :

$$DN(\lambda) = r(\lambda)E(\lambda).$$

The SFIM technique calculates high-resolution signal values  $DN(\lambda)_{sim}$  at wavelength  $\lambda$  as follows:

$$DN(\lambda)_{\text{sim}} = \frac{DN(\lambda)_{\text{low}} DN(\gamma)_{\text{high}}}{DN(\gamma)_{\text{mean}}},$$
(1)

where  $DN(\lambda)_{low}$  is the low-resolution signal at wavelength  $\lambda$ ;  $DN(\gamma)_{high}$  is the high-resolution signal at wavelength  $\gamma$  and  $DN(\gamma)_{mean}$  is the local mean of  $DN(\gamma)_{high}$  for the resolution element of the low spatial resolution image. The method assumes that  $DN(\lambda)$  and  $DN(\gamma)$  exhibit similar dependencies on surface topography. The resulting fused data preserve the information content in the original low-resolution image, independent of the spectral properties of the high-resolution image.

In [20], the SFIM algorithm was adapted to enhance the spatial resolution of brightness temperature (*T*b) fields of the Advanced Microwave Scanning Radiometer – Earth Observation System (AMSR-E) at 6.9 GHz (*C*-band) using the measurements at 36.5 GHz (Ka-band). Equation (1) was modified for the AMSR-E data as follows:

$$Tb_{\text{CHres}} = \frac{Tb_{\text{Corig}}Tb_{\text{Korig}}}{Tb_{\text{KLres}}},\tag{2}$$

where  $Tb_{\rm CHres}$  is the Tb radiation of the high-resolution C-band;  $Tb_{\rm Corig}$  is the Tb radiation of the original resolution C-band;  $Tb_{\rm Korig}$  is the Tb radiation of the original (high) resolution Ka-band;  $Tb_{\rm KLres}$  is Tb radiation of the low-resolution Ka-band, obtained by averaging values in those resolution elements that fall within the low-resolution C-band pixel. In fact, to apply the algorithm, the field of Tb measurements in the Ka-band ( $Tb_{36{\rm high}}$ ) is processed with a low-pass filter to generate the low-resolution Tb field at 36.5 GHz ( $Tb_{36{\rm low}}$ ) and the resulting ratio  $Tb_{36{\rm high}}/Tb_{36{\rm low}}$  is used to modulate the low-frequency measurements. In [15], the application of this method to enhance the resolution of soil moisture fields was explored, with the analyses of the resulting  $Tb_{\rm CHres}$  fields for the two geographical regions – the Amazon Delta and Lake Victoria in Equatorial Africa. However, the authors of the study did not discuss the applicability of the SFIM method, which differs fundamentally from its use for optical images, as it relies on the assumption that  $DN(\lambda)$  and  $DN(\gamma)$  exhibit similar dependencies on surface topography.

This study aims to modify the SFIM method to enhance the spatial resolution of Advanced Microwave Scanning Radiometer 2 (AMSR2) measurements at 6.9 GHz, utilizing the measurements at 36.5 GHz for the Arctic region, to facilitate the analysis of underlying surface properties.

#### Methodology

The *T*b of microwave radiation depends on both surface and atmospheric properties. In the absence of scattering, under the microwave approximation, the *T*b for horizontally (H) and vertically (V) polarized radiation ( $Tb^{H,V}$ ) can be expressed as:

$$Tb^{H,V} = T_a^{\ \uparrow} + \chi^{H,V} \cdot T_s \cdot e^{-\tau} + (1+\Omega) \cdot (T_a^{\ \downarrow} + e^{-\tau} \cdot T_c) \cdot e^{-\tau} \cdot (1-\chi^{H,V}), \quad (3)$$

where  $T_a^{\uparrow}$  and  $T_a^{\downarrow}$  are the *T*b of upwelling and downwelling atmospheric radiation;  $\tau$  is the atmospheric optical thickness in the observation direction  $\theta$ ;  $\chi^{H,V}$  is the effective emissivity for the *H*- and *V*-polarized radiation;  $T_c$  is the cosmic background radiation,  $T_c = 2.7 \, \text{K}$ ;  $T_s$  is the surface temperature;  $\Omega$  is a corrective term accounting for radiation scattered in the direction  $\theta$  from the incidence angles other than  $\theta$  [21]. Equation (3) is valid for the frequency range f from 1 to 100 GHz in the absence of the atmospheric scatterers with the characteristic sizes r exceeding  $\lambda/2\pi$  [22]. For diffusely reflecting surfaces at the angles around 50°, the corrective term  $\Omega$  can be neglected [23]. Numerical results indicate that under the Arctic atmospheric conditions, upwelling and downwelling atmospheric radiation can be considered the same and equal to  $T_a$ . The errors associated with this approximation are discussed in [24]. Neglecting the cosmic radiation attenuated by the double atmospheric layer, the expression simplifies to:

$$Tb^{H,V} = \chi^{H,V} \cdot e^{-\tau} (T_s - T_a) + T_a (1 + e^{-\tau}). \tag{4}$$

Equation (4) describes the Tb of the system radiation at different frequencies. The frequency-dependent functions are the effective emissivity and the interrelated atmospheric radiation  $T_a$  and its optical thickness  $\tau$ .

For the atmosphere with low values of the total water vapor content Q and total cloud liquid water content W, the atmospheric radiation is directly proportional to its optical thickness [25]:

$$T_a = T_0 \tau, \tag{5}$$

where  $T_0$  is a constant, and  $e^{-\tau}$  can be approximated as  $1 - \tau$ . Using these approximations, Equation (4) can be rewritten as:

$$Tb^{H,V} = \chi^{H,V} \cdot \left(1 - \frac{T_a}{T_0}\right) (T_s - T_a) + T_a \left(2 - \frac{T_a}{T_0}\right).$$
 (6)

According to Equation (6), the Tb of radiation is a function of the atmospheric parameters (via  $T_a$ ), surface temperature  $T_s$  and surface properties (via effective emissivity  $\chi^{H,V}$ ). The validity of using Equation (2) to modulate Tb at 6.9 GHz ( $Tb_{06}$ ) with Tb at 36.5 GHz ( $Tb_{36}$ ), as proposed in [15], depends on the accuracy of the assumption that  $Tb_{06high}/Tb_{06low} = Tb_{36high}/Tb_{36low}$ . Here,  $Tb_{06low}$  represents the measurements at 6.9 GHz with the original (low) resolution;  $Tb_{36high}$  denotes the measurements at 36.5 GHz of the original (high) resolution, and  $Tb_{36low}$  is the low resolution Tb at 36.5 GHz, averaged over the resolution element (S) of the 6.9 GHz measurements. The error of this assumption varies depending on the study region and the characteristics of the underlying surface.

Deviations (variations) of  $Tb_{high}$  from the mean  $Tb_{low}$  within S can be expressed as:

$$\Delta T b^{H,V} = \Delta \chi^{H,V} \frac{\partial T b^{H,V}}{\partial \chi^{H,V}} + \Delta T_S \frac{\partial T b^{H,V}}{\partial T_S} + \Delta T_a \frac{\partial T b^{H,V}}{\partial T_a}.$$
 (7)

The derivatives  $\frac{\partial Tb^{H,V}}{\partial T_a}$ ,  $\frac{\partial Tb^{H,V}}{\partial \chi^{H,V}}$  and  $\frac{\partial Tb^{H,V}}{\partial T_s}$  at 6.9 and 36.5 GHz differ significantly. Notably, variations in  $\Delta T_a$  are significant at 36.5 GHz but can be neglected at 6.9 GHz. To express  $\Delta Tb_{06\text{high}}$  as a function of  $\Delta Tb_{36\text{high}}$ , the following conditions must be satisfied within the resolution element S:

$$\Delta \chi^{H,V} \frac{\partial T^{H,V}}{\partial \chi^{H,V}} \gg \Delta T_a \frac{\partial T^{H,V}}{\partial T_a}, \ \Delta \chi^{H,V} \frac{\partial T^{H,V}}{\partial \chi^{H,V}} \gg \Delta T_S \frac{\partial T^{H,V}}{\partial T_S}. \tag{8}$$

If these conditions are not satisfied, modulating the  $Tb_{06\text{low}}$  measurements with the  $Tb_{36\text{high}}$  measurements will be impossible, since  $\Delta Tb_{36\text{high}}$  values will depend on the atmospheric parameters or surface temperature, and not on the effective emissivity determined by the dielectric properties of the surface. Even when conditions (8) are satisfied,  $Tb^{06}_{\text{high}}$  cannot be expressed as  $(Tb_{06\text{low}} \cdot Tb_{36\text{high}})/Tb_{36\text{low}}$  (Equation (2)) for any surface, since, in general,  $\frac{\partial Tb_{06}}{\partial \chi_{36}} \neq \frac{\partial Tb_{36}}{\partial \chi_{36}}$  and  $\Delta \chi_{06} \neq \Delta \chi_{36}$ .

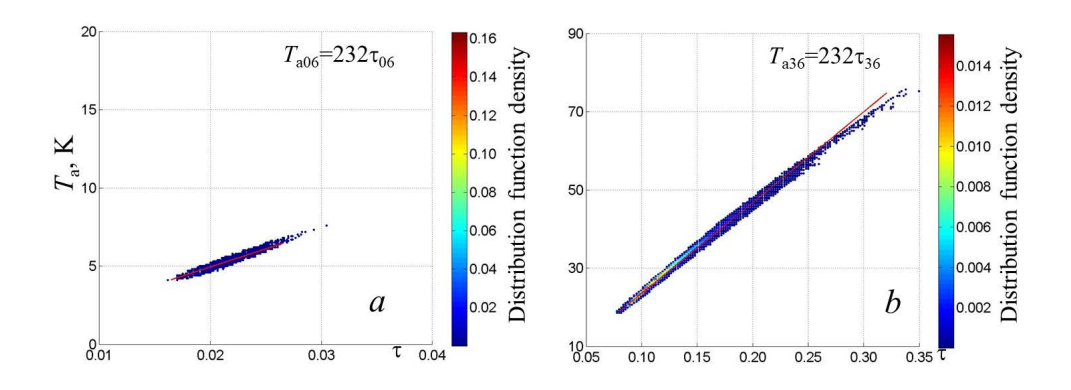
The objective of this study was to find the conditions under which  $\Delta Tb_{06high}$  can be expressed through  $\Delta Tb_{36high}$  to enhance the spatial resolution of the underlying surface parameters using *C*-band channels. Numerical calculations of *Tb* were performed for open water (*OW*) and sea ice (*SI*) under non-scattering Arctic atmospheric conditions, using Equation (4) and the ERA5 reanalysis data for the atmospheric parameters (humidity, cloud liquid water, pressure and temperature) and surface temperature  $T_s$ . Effective emissivities  $\chi^{H,V}$  were obtained using the method described in [26]. Based on these calculations, all the three components in Equation (7) were numerically assessed for the Arctic Sea conditions. The classification of the surface into *OW/SI* types was conducted done with the sea ice concentration retrieval algorithm applied to the AMSR2 measurement data [27], with the sea ice type classification with the method, described in [28].

#### Results and discussion

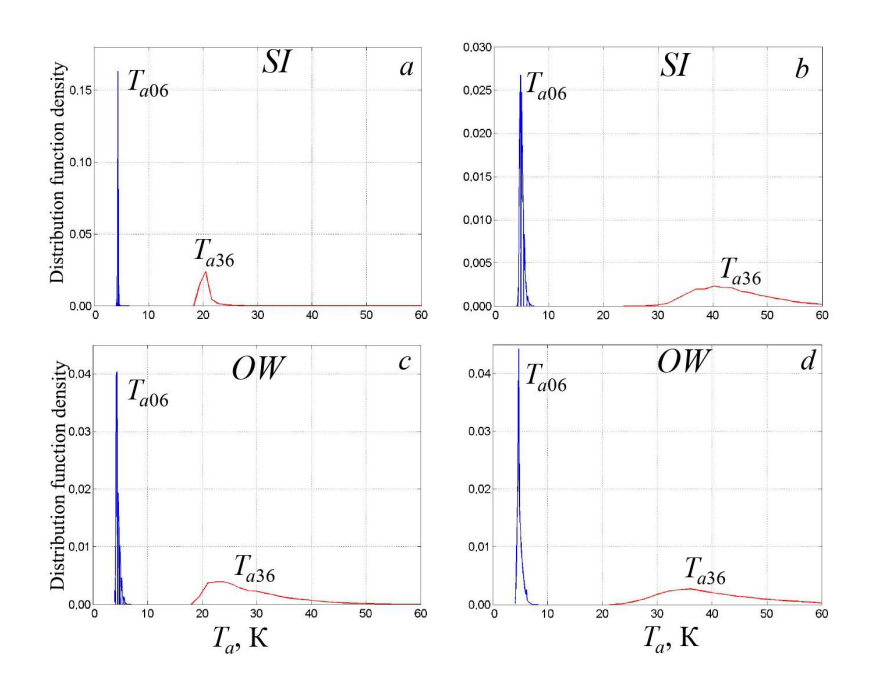
Numerical calculations of the atmospheric microwave radiation  $T_a$  and atmospheric optical thickness  $\tau$  provided values for the coefficient  $T_0$  in Equation (5) for the frequencies of 6.9 and 36.5 GHz. Fig. 1 demonstrates the applicability of the approximation (5) under the Arctic conditions throughout the whole year. As the atmospheric water content parameters (Q and/or W) increase,  $\tau$  rises, and when  $\tau_{36}$  exceeds  $\sim 0.2$  ( $T_{a36} \sim 45$  K), Equation (5) starts to be invalid. Under the Arctic conditions, such  $\tau_{36}$  values occur over the sea ice and coastal land areas only during warmer months (May to October).

Under conditions where approximation (5) is valid, Tb and the partial derivatives  $\frac{\partial Tb^{H,V}}{\partial T_a}$ ,  $\frac{\partial Tb^{H,V}}{\partial \chi^{H,V}}$  and  $\frac{\partial Tb^{H,V}}{\partial T_s}$  were calculated using Equation (6), with the other two parameters fixed. The variations  $\Delta T_a$ ,  $\Delta T_s$  and  $\Delta \chi^{H,V}$  were determined to estimate  $\Delta Tb_{06\text{high}}$  and  $\Delta Tb_{36\text{high}}$ .  $\Delta T_a$ ,  $\Delta T_s$  and  $\Delta \chi^{H,V}$  were defined as the root-

mean-square deviations  $\sigma$  within the monthly datasets. While such estimates do not directly represent the variations within the resolution element S, they provide the measure of the parameter variability in the region over the specified time interval.



**F i g. 1.** Dependence of the atmospheric microwave radiation  $T_a$  on its optical thickness  $\tau$  in the Arctic conditions during a year at the 6.9 (a) and 36.5 (b) GHz frequencies

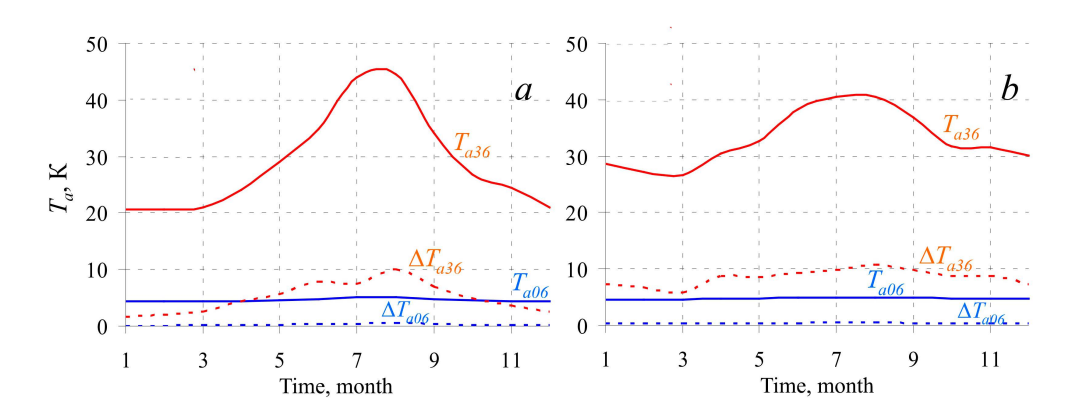


**F i g. 2.** Probability distribution functions for the  $T_{a06}$  and  $T_{a36}$  over the sea ice (a, b) and sea water (c, d) in January (a, c) and July (b, d)

## 1. $\Delta Tb_{06}$ and $\Delta Tb_{36}$ dependence on atmospheric radiation

Fig. 2 illustrates the typical distributions of  $T_{a06}$  (atmospheric radiation at 6.9 GHz) and  $T_{a36}$  (atmospheric radiation at 36.5 GHz) for summer (July) and winter (January) months over sea ice SI and open water OW.

The variability of  $T_{a06}$  parameter is low (0.1–0.5K) independently of the underlying surface types or seasons. In contrast,  $T_{a36}$  exhibits low variability (approximately a few kelvins) only during the winter season (November to March) over sea ice. The dependence of the average values of  $T_{a06}$  and  $T_{a36}$ , along with their variability ( $\Delta T_{a06}$  and  $\Delta T_{36}$ ), on the month is presented in Fig. 3.



**F i g. 3.** Average values of  $T_{a06}$  and  $T_{a36}$ , and their variability  $\Delta T_{a06}$  and  $\Delta T_{36}$  over sea ice (a) and sea water (b) depending on the month of a year

From Equation (6) it follows:

$$\frac{\partial Tb^{H,V}}{\partial T_a} = (\chi^{H,V} - 1)\frac{2T_a}{T_0} + (2 - \chi^{H,V}(1 + \frac{T_s}{T_0})).$$

The values of  $\frac{\partial Tb^{H,V}}{\partial T_a}$  are nearly constant at both frequencies, although a slight decrease is observed at 36.5 GHz with increasing  $T_{a36}$ . At 6.9 GHz,  $\frac{\partial Tb^{H,V}}{\partial T_a} \sim 1.2-1.7$ , depending on the surface type. Given extremely low variability of  $\Delta T_{a06}$  (0.1–0.5 K),  $\Delta T_{a06} \frac{\partial Tb^{H,V}}{\partial T_a}$  does not exceed 0.8 K. Since  $\Delta T_{a06}$  within a resolution element S is evidently smaller than across the entire Arctic, it can be assumed that  $\Delta T_{a06} \frac{\partial Tb^{H,V}}{\partial T_a} = 0$ .

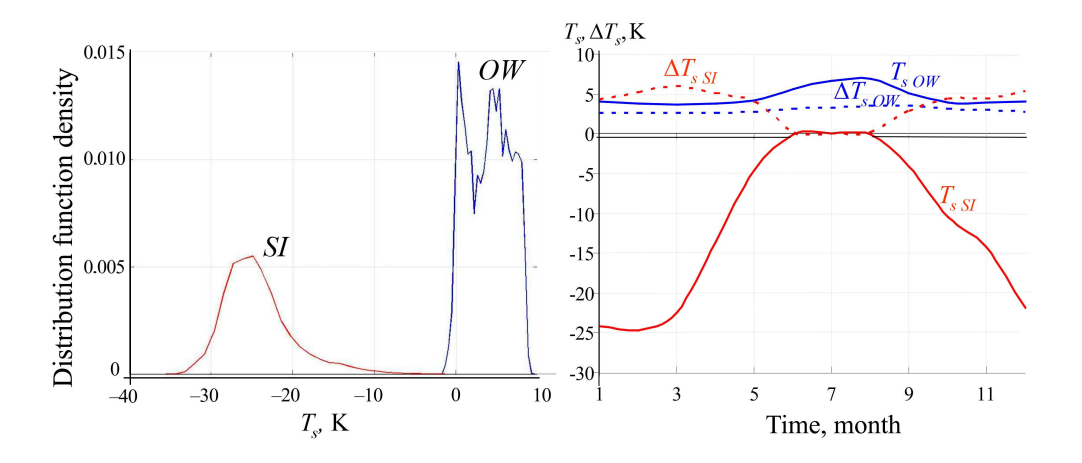
At 36.5 GHz,  $\frac{\partial Tb^{H,V}}{\partial T_a} \sim 1$  over sea ice and  $\sim 1.5$  over open water. From November to March, over sea ice,  $\Delta T_{a36} \sim 2-4$  K, while for the rest of the year and over seawater year-round,  $\Delta T_{a36} \sim 5-10$  K. Consequently,  $\Delta T_{a36} \frac{\partial Tb^{H,V}}{\partial T_a}$  varies from 2 to 15 K, depending on the season and underlying surface type. At this, over sea ice,  $\Delta T_{a36}$  can be calculated using the AMSR2 Level 1R satellite product.

## 2. $\Delta Tb_{06}$ and $\Delta Tb_{36}$ dependence on surface temperature

$$\frac{\partial T\mathbf{b}^{H,V}}{\partial T_S} = \chi^{H,V} (1 - \frac{T_a}{T_0})).$$

The values of  $\frac{\partial Tb^{H,V}}{\partial T_s}$  are determined mainly by the values of  $\chi^{H,V}$ , resulting in the values approximately twice as high for sea ice as for seawater (depending on polarization). At 36.5 GHz, they are an order of magnitude higher than at 6.9 GHz, amounting to  $\sim 0.1-0.2$  K/K. The high variability of  $T_{a36}$  and  $\chi^{H,V}_{36}$  compared to  $T_s$  explains why 36.5 GHz channels are never used for surface temperature retrieval. The root-mean-square deviation of  $T_s$  ( $\Delta T_s$ ), calculated for monthly data across the Arctic for OW and SI, is presented in Fig. 4, b.

For sea water the  $T_s$  variability in Arctic seas remains nearly constant ( $\sim 3-4$  K) through a year, while for sea ice in winter,  $\Delta T_s \sim 5-7$  K. Consequently,  $\Delta T_s \frac{\partial Tb^{H,V}}{\partial T_s}$  at 6.9 GHz does not exceed 0.2 K, and at 36.5 GHz, it is up to 1 K.



**F** i g. 4. Probability distribution functions for the  $T_s$  of open water (OW) and sea ice (SI) in January (a);  $T_s$  average values and their variability  $\Delta T_s$  depending on the month of a year (b)

# 3. $\Delta Tb_{06}$ and $\Delta Tb_{36}$ dependence on effective emission coefficient

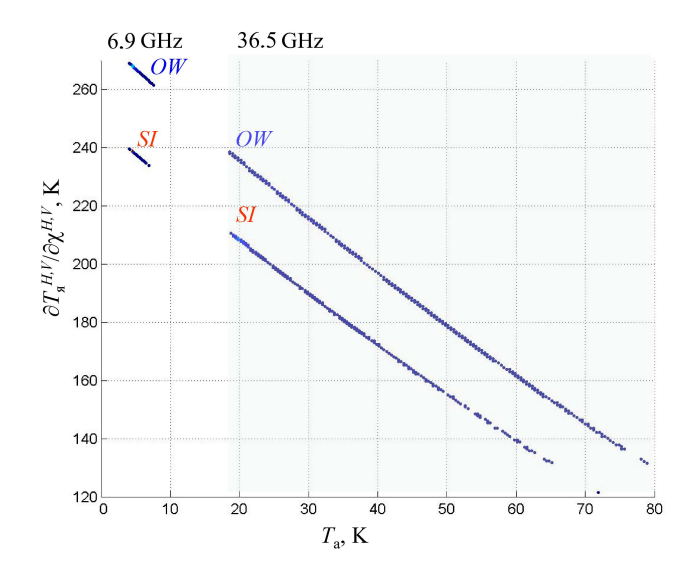
$$\frac{\partial Tb^{H,V}}{\partial \chi^{H,V}} = \left(1 - \frac{T_a}{T_0}\right) (T_s - T_a). \tag{9}$$

Equation (9), derived from Equation (6), explains the reduced sensitivity of the signal to surface properties as the atmospheric radiation increases. At 6.9 GHz,  $T_a$  is nearly constant (see Fig. 3), so  $\frac{\partial Tb^{H,V}}{\partial \chi^{H,V}}$  is primarily determined by the parameter  $T_s$  and is independent of the atmospheric conditions. At 36.5 GHz,

 $\frac{\partial Tb^{H,V}}{\partial \chi^{H,V}}$  depends on both  $T_s$  and  $T_a$ . However, in winter conditions (October to May), when  $T_{a36}$  does not exceed 30 K,  $\frac{\partial Tb^{H,V}}{\partial \chi^{H,V}}$  at 6.9 GHz can be expressed as a function of  $\frac{\partial Tb^{H,V}}{\partial \chi^{H,V}}$  at 36.5 GHz:

$$\frac{\partial Tb_{06}^{H,V}}{\partial \chi_{06}^{H,V}} \sim \beta \frac{\partial Tb_{36}^{H,V}}{\partial \chi_{36}^{H,V}}.$$
 (10)

Numerical calculations for winter conditions, with typical  $T_a$  values ( $\sim 5$  K at 6.9 GHz and 20–30 K at 36.5 GHz), show that  $\frac{\partial Tb^{H,V}}{\partial \chi^{H,V}}$  at 6.9 GHz is  $\sim 265$  K over seawater and  $\sim 240$  K over sea ice. At 36.5 GHz, the values of  $\frac{\partial Tb^{H,V}}{\partial \chi^{H,V}}$  are  $\sim 200-235$  K over seawater and  $\sim 170-205$  K over sea ice (Fig. 5). The coefficient  $\beta$  is  $\sim 1.2$ , increasing slightly with  $T_a$  ( $\beta \sim 1.2$  at  $T_{a36} \sim 20-25$  K,  $\beta \sim 1.25$  at  $T_{a36} \sim 25-30$  K).



**F i g. 5.** Sensitivity of Tb to the effective emission coefficient of seawater and sea ice as a function of atmospheric radiation  $T_a$ . The curves on the left side of the Figure are for the sensitivity at the 6.9 GHz, on the right side (gray background) – at the 36.5 GHz

Due to such high sensitivity of Tb to the surface emission coefficient, even small variations in  $\chi$  ( $\sim$  0.01) significantly contribute to  $\Delta Tb$ .

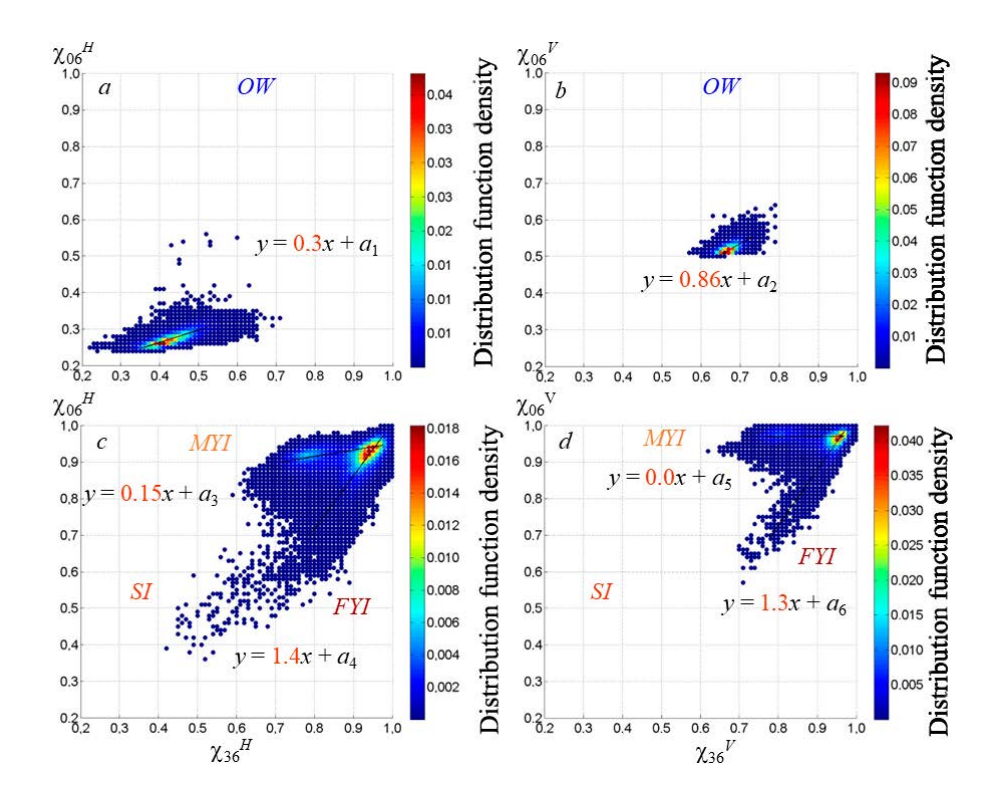


**Fig. 6.** Dependence of  $\chi^{06}$  on  $\chi^{36}$  for ocean water OW(a, b), and first-year (FY) and multi-year (MY) sea ice SI(c, d) at horizontal (H)(a, c) and vertical (V)(b, d) polarizations

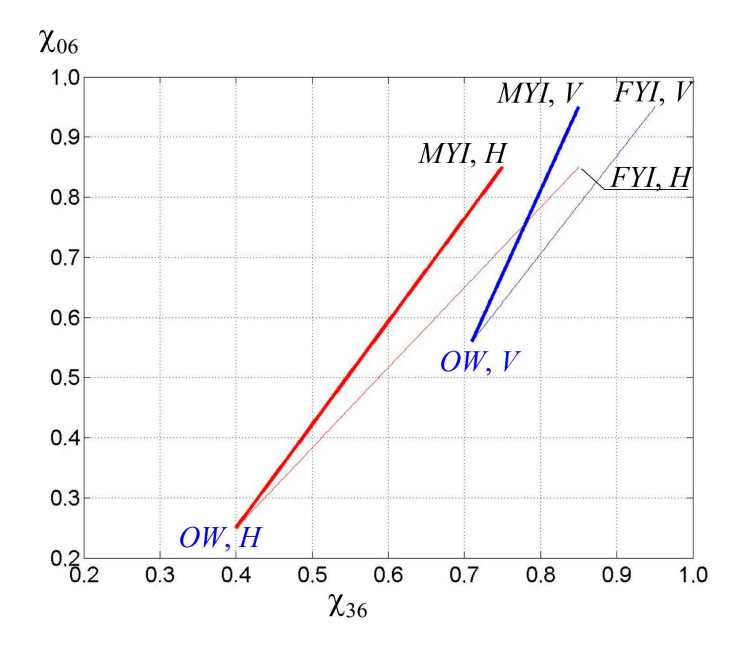
The variability of surface characteristics affects the effective emission coefficient differently at different frequencies. To establish the relationship  $\Delta\chi_{06} = f(\Delta\chi_{36})$ , arrays of sea ice emissivity coefficients were analyzed for the surfaces, classified as First Year Ice (*FYI*), Multi-Year Ice (*MYI*), and open water OW – across the whole Arctic during the cold period (October 2019 to May 2020). OW/SI classification was performed using the algorithm [27], and the sea ice type classification using the algorithm [28]. The dependence of  $\chi_{06}$  on  $\chi_{36}$  for sea ice and seawater at horizontal and vertical polarizations is presented in Fig. 6, with point clouds distinguishing *FYI* and *MYI* for sea ice. These relationships were approximated by linear functions  $\chi_{06} = \alpha_i \chi_{36} + a_i$  for each polarization and surface type. For a surface with sea ice concentration (*SIC*) ranging from 0 to 1, the effective emissivity is determined as:

$$\chi_{06}^{H,V} = SIC\chi_{06}^{SI} + (1 - SIC)\chi_{06}^{OW},$$

$$\chi_{36}^{H,V} = SIC\chi_{36}^{SI} + (1 - SIC)\chi_{36}^{OW},$$
(11)

where  $\chi_{06}^{OW}$  and  $\chi_{36}^{OW}$  represent the effective emission coefficients for open water at 6.9 and 36.5 GHz, respectively (shown as point clouds in Fig. 6, a, b), while  $\chi_{06}^{SI}$  712 PHYSICAL OCEANOGRAPHY VOL. 32 ISS. 5 (2025)

and  $\chi_{36}^{SI}$  denote the effective emission coefficients for sea ice at 6.9 and 36.5 GHz, respectively (shown as point clouds in Fig. 6, *c*, *d*). These relationships (11) enable the construction of dependencies of  $\chi_{06}$  on  $\chi_{36}$  for arbitrary *SIC* values for both *FYI* and *MYI*. Fig. 7 illustrates the dependencies of  $\chi_{06}$  on  $\chi_{36}$  for surfaces with varying *SIC* values: red lines represent *H*-polarization and blue lines represent *V*-polarization. Thin lines correspond to *FYI* with *SIC* = 1, where  $\chi_{06}^{H} = 0.85$ ,  $\chi_{36}^{H} = 0.85$ ,  $\chi_{36}^{H} = 0.85$ ,  $\chi_{36}^{H} = 0.95$ , thick lines correspond to *MYI* with *SIC* = 1, where  $\chi_{06}^{H} = 0.85$ ,  $\chi_{06}^{V} = 0.95$ ,  $\chi_{36}^{H} = 0.75$ ,  $\chi_{36}^{V} = 0.85$ . These values align with the maxima of the distribution functions for  $\chi$  for *FYI* and *MYI*, as reported in [26]. For OW(SIC = 0), the emission coefficients are  $\chi_{06}^{H} = 0.25$ ,  $\chi_{06}^{V} = 0.56$ ,  $\chi_{36}^{H} = 0.4$ ,  $\chi_{36}^{V} = 0.71$ .



**F** i.g. 7. Dependence of  $\chi_{06}$  on  $\chi_{36}$  for a surface with an arbitrary *SIC* value at *H*- (red lines) and *V*- (blue lines) polarizations: first-year ice (*FYI*) with the values at SIC = 1:  $\chi_{06}{}^H = 0.85$ ,  $\chi_{06}{}^V = 0.95$ ,  $\chi_{36}{}^H = 0.85$ ,  $\chi_{36}{}^V = 0.95$  (thin lines), multi-year ice (*MYI*) with the values at SIC = 1:  $\chi_{06}{}^H = 0.85$ ,  $\chi_{06}{}^V = 0.95$ ,  $\chi_{36}{}^H = 0.75$ ,  $\chi_{36}{}^V = 0.85$  (thick lines). *OW* points correspond to  $\chi$  for seawater at SIC = 0:  $\chi_{06}{}^H = 0.25$ ,  $\chi_{06}{}^V = 0.56$ ,  $\chi_{36}{}^H = 0.4$ ,  $\chi_{36}{}^V = 0.71$ 

The regression equations from Fig. 6 and Equations (11) allow to express  $\Delta \chi_{06}$  through  $\Delta \chi_{36}$  for different conditions as follows:

$$\Delta \chi_{06} = \alpha \Delta \chi_{36}$$

where  $\alpha$  is a coefficient whose values for different sea surface types are provided in the Table. The  $\alpha$  values for surfaces with 0 < SIC < 1 correspond to conditions where the distribution functions of  $\chi_{06}$  and  $\chi_{36}$  for FYI and MYI reach their maxima [26].

Coefficient $\alpha$ relating $\Delta\chi_{06}$ to	$\Delta\chi_{36}$ for various surface types
at different	polarizations

Type of surface	SIC	α	α	
	SIC	Н	V	
Seawater	0	0.30	0.86	
FYI	1	1.40	1.30	
MYI	1	0.15	0.00	
FYI	[0, 1)	1.30	1.60	
MYI	[0, 1)	1.70	2.80	

Although sea ice concentration does not change abruptly in practice, for practical applications (and taking into account the the SIC retrieval errors), the  $\alpha$  coefficients for SIC = 1 can be applied for sea ice concentrations of 0.9-1, and those for SIC = 0 can be used for sea ice concentrations of 0–0.2.

The Table shows that improving the spatial resolution of Tb fields at 6.9 GHz for vertical polarization in MYI areas is not possible, as  $\Delta\chi_{06}$  does not correlate with  $\Delta\chi_{36}$ . At horizontal polarization, slight modulation of  $Tb_{06}{}^H$  is possible when there are significant changes in  $\Delta\chi_{36}$ , since  $\Delta Tb_{06}{}^H$  is approximately five times smaller than  $\Delta Tb_{36}{}^H$  (1.2·0.15). For other surface types, the contribution of effective emissivity variability to  $\Delta Tb_{06}$  can be expressed as:

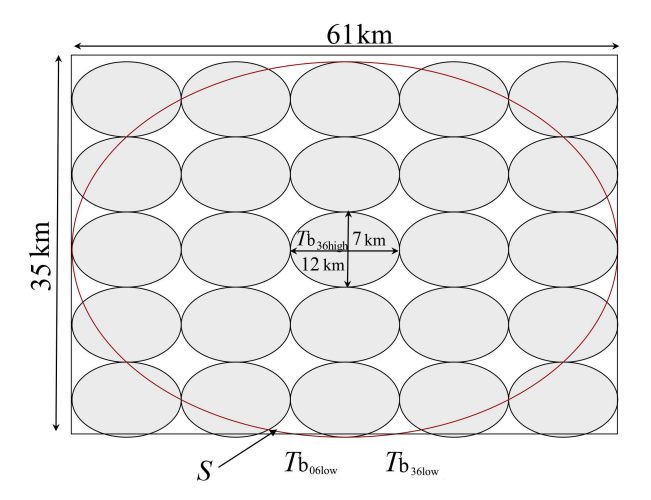
$$\Delta T b_{06}^{H,V} = \Delta \chi_{06}^{H,V} \frac{\partial T_{06}^{H,V}}{\partial \chi_{06}^{H,V}} \sim \alpha \Delta \chi_{36}^{H,V} \beta \frac{\partial T_{36}^{H,V}}{\partial \chi_{26}^{H,V}} \sim 1.2 \alpha \Delta T b_{36}^{H,V}.$$

A change in SIC by 0.1, depending on the sea ice type, results in variations in  $\Delta\chi_{36} \frac{\partial T_{36}^{H,V}}{\partial\chi_{36}^{H,V}}$  of at least 5–10 K, depending on the sea surface state. This means that, even in summer conditions with possible essential atmospheric variability within a pixel S, the impact of sea ice concentration on  $\Delta Tb_{36}$  is comparable to or exceeds that of the atmospheric parameters (see Fig. 3). Consequently, a 0.1 change in SIC induces  $\Delta Tb_{06}$  of  $\sim 8-30$  K, indicating that the sea ice/ sea water contrasts in  $Tb_{06}$  fields are significantly more prominent than in  $Tb_{36}$  fields.

#### Method application

The microwave radiometer AMSR2 on the GCOM-W1 satellite measures vertically (V) and horizontally (H) polarized microwave radiation at seven frequencies – 6.95; 7.3; 10.65; 18.7; 23.8; 36.5 and 89 GHz – with spatial resolutions

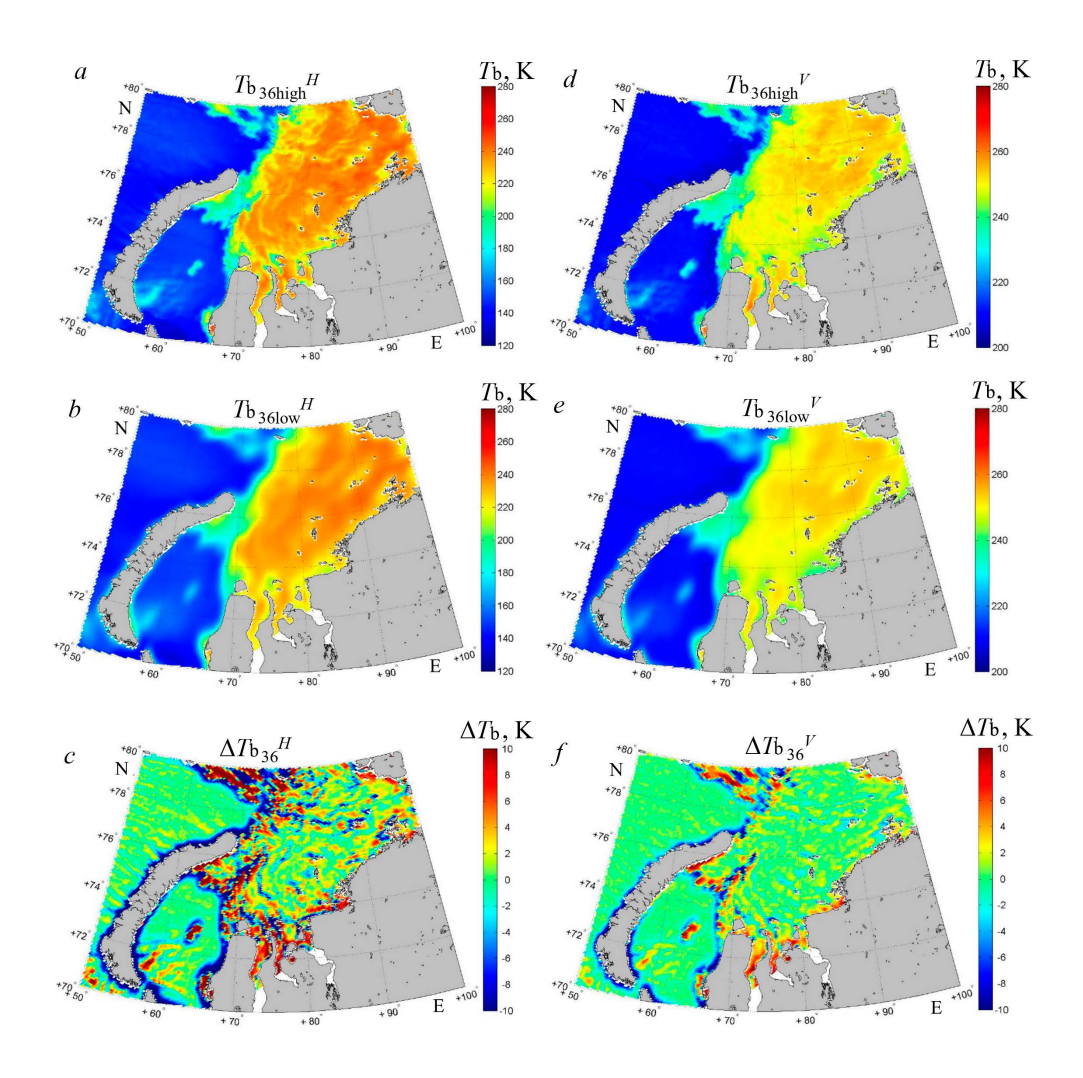
ranging from  $35 \times 61$  km at 6.9 GHz to  $3 \times 5$  km at 89 GHz. The pixel size is  $5 \times 5$  km at 89 GHz and  $10 \times 10$  km for the other channels. Enhancing the spatial resolution of low-frequency channels using the AMSR2 high-frequency channel measurements, as described in [19] and applied in [20], is technically straightforward for Level 1R data. These data include the *Tb* measurements at higher frequencies with different levels of averaging corresponding to the resolutions of low-frequency channels (resampling data). Specifically, the measurements at 36.5 GHz in the Level 1R satellite product are provided at their original resolution and as the three additional datasets averaged over the resolution elements of the 23.8, 10.65, and 6.95 GHz channels. Fig. 8 schematically illustrates the resolution element *S* for the 6.95 GHz channel, composed of resolution elements at the 36.5 GHz channel.



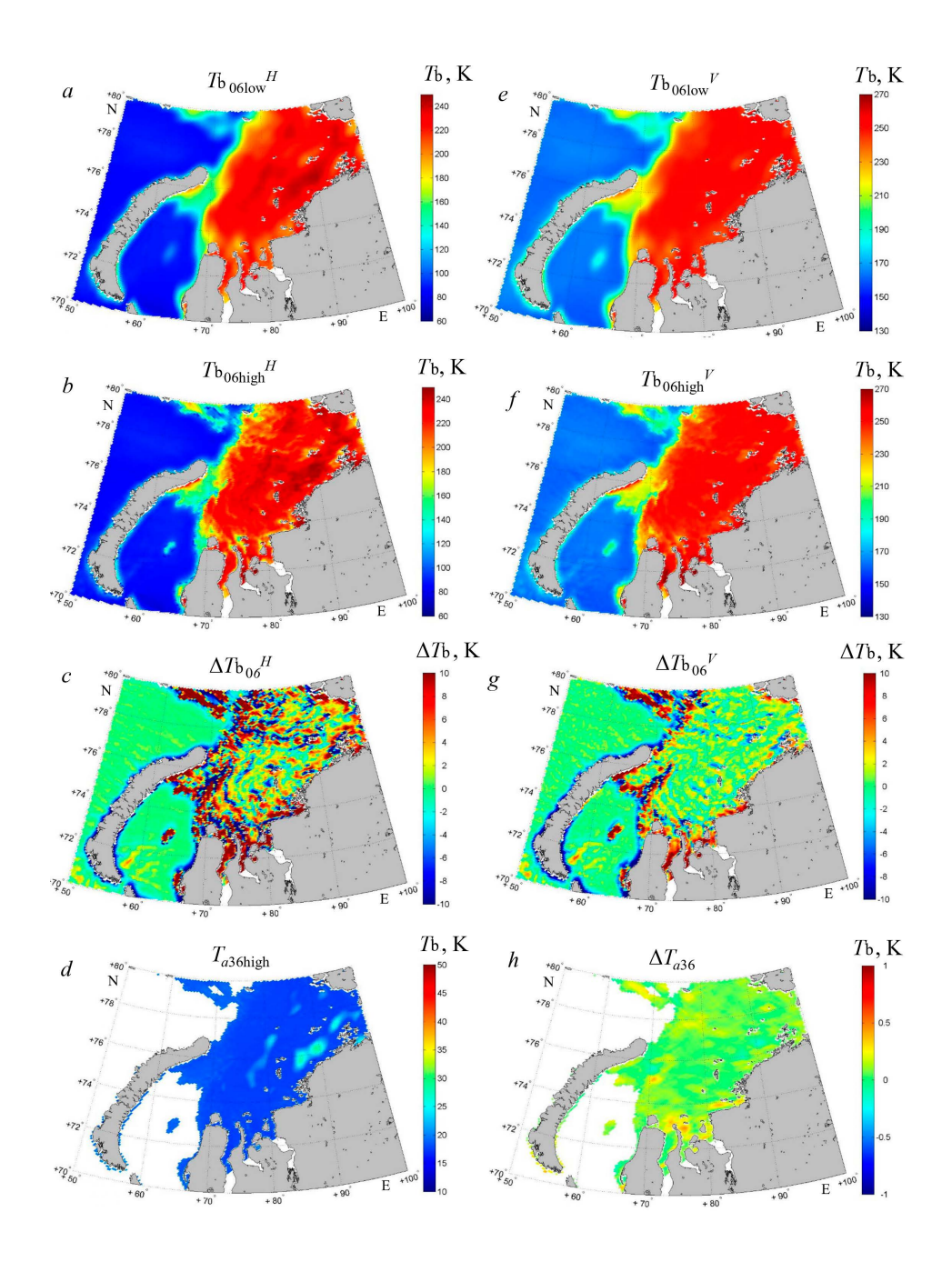
**F i g. 8.** Scheme for averaging the *T*b measurements at 36.5 GHz to relate these measurements to the resolution of measurements at 6.9 GHz (resolution element *S*) in the AMSR2 Level 1R satellite product

Since the measurement recording frequency aligns with a pixel size of  $10 \times 10$  km,  $\Delta Tb_{36}$  within a pixel is the difference between  $Tb_{36\text{high}}$  and  $Tb_{36\text{low}}$ .

Based on the findings obtained from the previous section, Equation (2) from [20] is not suitable for enhancing the spatial resolution of AMSR2 measurements at 6.9 GHz when studying the surface properties of sea ice or seawater. In general,  $\Delta T$ b<sub>06</sub> variability within the low-resolution pixel S cannot be directly expressed through  $\Delta T$ b<sub>36</sub> variability, as the variability of the atmospheric radiation at 36.5 GHz ( $\Delta T$ a<sub>36</sub>) cannot be neglected in Equation (7). While it may be assumed that  $\Delta T$ a<sub>36</sub> is negligible during the cold season with low atmospheric water vapor and cloud liquid water content, the error of this assumption for any arbitrary underlying surface types cannot be quantitatively assessed.



**F** i g. 9. *T*b fields (AMSR2 Level 1R satellite product) measured by the AMSR2 radiometer at *H*- (*left*) and *V*- (*right*) polarizations at the 36.5 GHz frequency over the Kara Sea on November 17, 2024: original spatial resolution –  $Tb_{36high}^{H}(a)$  and  $Tb_{36high}^{V}(d)$ ; resolution of the 6.9 GHz channels –  $Tb_{36low}^{H}(b)$  and  $Tb_{36low}^{V}(e)$ ;  $\Delta Tb_{36}^{H} = Tb_{36high}^{H} - Tb_{36low}^{H}(c)$  and  $\Delta Tb_{36}^{V} = Tb_{36high}^{V} - Tb_{36low}^{V}(f)$ 



**F i g. 10.** *T*b fields (AMSR2 Level 1R satellite product) measured by the AMSR2 radiometer at *H*- (a, b, c) and *V*- (e, f, g) polarizations at the 6.9 (a – c, e – g) and 36.5 (d, h) GHz frequencies over the Kara Sea (a, d) on November 17, 2024 (a, d) and calculated with the enhanced spatial resolution (b, f): original spatial resolution –  $Tb_{06low}^H(a)$ ,  $Tb_{06low}^V(e)$  and  $T_{a36high}(d)$ ; enhanced resolution –  $Tb_{06high}^H(b)$ ,  $Tb_{06high}^V(f)$ ; difference between the fields of enhanced  $\Delta Ta_{06}^H(c)$  and low  $\Delta Ta_{06}^V(g)$  resolutions; variability of atmospheric radiation  $\Delta Ta_{36} = T_{a36high} - T_{a36low}(h)$ 

 $\Delta T_{\rm a36}$  over the sea ice can be calculated using the AMSR2 measurement data [24]. Fig. 9 presents the AMSR2 Tb fields at 6.9 and 36.5 GHz channels (V and H polarizations) at their original spatial resolutions (AMSR2 Level 1R satellite product) over the Kara Sea. Fig. 10 displays Tb fields at 6.9 GHz with the enhanced resolution, with the fields of  $\Delta T_{36}$  and  $\Delta T_{06}$ . Here,  $\Delta T_{36}$  is calculated as the difference between Tb<sub>36high</sub> and Tb<sub>36low</sub> (both provided in the Level 1R product), and  $\Delta T_{06}$  is determined using Equation (10).

The calculated variations of atmospheric radiation  $\Delta T_{a36}$  over sea ice, which do not exceed 0.3 K in absolute value (Fig. 10, h), enable the application of Equation (10) to calculate  $Tb_{06\text{high}}^H$  and  $Tb_{06\text{high}}^V$ . This calculation uses  $\alpha$  coefficients specific for FYI in the Kara Sea at SIC=1, open water at SIC=0, and the sea surface partially covered with sea ice at 0 < SIC < 1. SIC was determined using an algorithm based on AMSR2 measurements at 89 GHz [27], while the sea ice type was identified using a threshold method described in [28], leveraging the measurement data at 36.5 and 18.7 GHz. The resolution of the sea ice concentration and sea ice type fields is at least as high as that of the 36.5 GHz measurements. In this case, a priori knowledge of the seasonal absence of multi-year ice in the Kara Sea simplifies the sea ice type determination.

The areas near coastlines require special consideration. The antenna horns at 6.9 and 36.5 GHz capture significantly different land areas near the coast, and these areas vary for ascending and descending satellite passes. Consequently, enhancing the spatial resolution near the coast is possible only when the satellite pass direction is from land to sea, not vice versa.

#### Conclusion

This work considers the possibility of enhancing the spatial resolution of the AMSR2 measurements on C-band channels (6.9 GHz) using the measurements at 36.5 GHz to study the surface parameters of the Arctic seas. Physical modeling of the Tb radiation for the ocean—sea ice—atmosphere system demonstrated that the direct application of the SFIM method, which relies on the Tb<sub>36high</sub>/Tb<sub>36low</sub> ratio to modulate low-frequency AMSR2 measurements, is not applicable for any arbitrary underlying surfaces and atmospheric conditions. A new approach was proposed for the Arctic seas, partially or fully covered with the sea ice, enabling the calculation of high resolution  $Tb_{06\text{high}}$  fields using the AMSR2  $Tb_{36\text{high}}$  and  $Tb_{36\text{low}}$ measurements (Level 1R satellite product) based on surface type (first-year, multiyear ice, seawater or surfaces with 0 < SIC < 1). The accuracy and applicability of this approach are primarily depend on the variability of the atmospheric water parameters within the low-resolution element S of the C-band measurements. These parameters significantly influence the Tb of the atmospheric microwave radiation at 36.5 GHz ( $T_{a36}$ ) and do not affect the Tb of the atmospheric microwave radiation at 6.9 GHz ( $T_{a06}$ ).

Since the method for estimating  $T_{a36}$  enables to calculate the  $\Delta T_{a36}$  in the element S when the surface is the sea ice, the possibility of enhancing the spatial resolution of measurements in C-band over the sea ice can be easily assessed. When  $\Delta T_{a36}$  does not exceed radiometric noise,  $Tb_{06high}$  over the first-year ice can be calculated as  $Tb_{06low} + 1.2 \cdot \alpha \cdot \Delta T_{836}$ , with  $\alpha = 1.3$  for H-polarization and  $\alpha = 1.6$  for V-polarization.

Over seawater, the  $\alpha$  coefficients are significantly smaller, with values of 0.3 for H-polarization and 0.86 for V-polarization. These values depend on the model, used for the sea surface emission coefficient dependence on sea surface wind speed, and they may change under strong wind conditions.

For multi-year ice, enhancing the spatial resolution of the *C*-band measurements at *V*-polarization using this approach is not possible, since the variations in the effective emission coefficient at 6.9 GHz for vertically polarized radiation are too small and uncorrelated with the variations in  $\chi$  at 36.5 GHz. However, at *H*-polarization, slight modulation of  $Tb_{06}^{\ H}$  is possible for the surfaces with significant  $\Delta\chi$  ( $\Delta T \pi_{36}$ ), resulting in  $\Delta T b_{06}^{\ H}$  approximately five times smaller than  $\Delta T b_{36}^{\ H} (1.2 \cdot 0.15)$ .

The proposed approach is applicable in the Arctic conditions from October to May and requires prior retrievals of the sea surface type and sea ice concentration. Such retrievals explore measurement channels with a spatial resolution equal to or higher than that of the 36.5 GHz channels. Consequently, the procedures for the surface type classification should not degrade the spatial resolution.

This method can be applied to develop the new sea ice concentration retrieval algorithms, as the 6.9 GHz channels are typically not used for *SIC* retrievals due to their low spatial resolution. It can also be explored for the sea ice drift retrievals. Extending the ability to estimate the atmospheric radiation variability at 36.5 GHz over both sea ice and sea water would further broaden the scope of the method for obtaining the sea surface wind fields with higher spatial resolution.

#### REFERENCES

- 1. Zabolotskikh, E.V. and Chapron, B., 2017. Atmospheric Total Water Vapor Content Retrieval Using Satellite Microwave Radiometer Measurements of AMSR2. *Sovremenniye Problemy Distantsionnogo Zondirovaniya Zemli iz Kosmosa*, 14(1), pp. 207-215. https://doi.org/10.21046/2070-7401-2017-14-1-207-215 (in Russian).
- Greenwald, T.J., Stephens, G.L., Vonder Haar, T.H. and Jackson, D.L., 1993. A Physical Retrieval of Cloud Liquid Water over the Global Oceans Using Special Sensor Microwave/Imager (SSM/I) Observations. *Journal of Geophysical Research: Atmospheres*, 98(D10), pp. 18471-18488. https://doi.org/10.1029/93JD00339
- 3. Wentz, F.J., Gentemann, C., Smith, D. and Chelton, D., 2000. Satellite Measurements of Sea Surface Temperature through Clouds. *Science*, 288(5467), pp. 847-850. https://doi.org/10.1126/science.288.5467.847
- 4. Comiso, J.C., 2009. Enhanced Sea Ice Concentrations and Ice Extents from AMSR-E Data. *Journal of the Remote Sensing Society of Japan*, 29(1), pp. 199-215. https://doi.org/10.11440/rssj.29.199
- Xing, D., Hou, J., Huang, C. and Zhang, W., 2022. Estimation of Snow Depth from AMSR2 and MODIS Data Based on Deep Residual Learning Network. *Remote Sensing*, 14(20), 5089. https://doi.org/10.3390/rs14205089
- 6. Lu, M., Hoang, K.O. and Kumarasiri, A.D.T.N., 2024. Temperature Effects in AMSR2 Soil Moisture Products and Development of a Removal Method Using Data at Ascending and Descending Overpasses. *Remote Sensing*, 16(9), 1606. https://doi.org/10.3390/rs16091606
- 7. Lenti, F., Nunziata, F., Estatico, C. and Migliaccio, M., 2013. On the Spatial Resolution Enhancement of Microwave Radiometer Data in Banach Spaces. *IEEE Transactions on Geoscience and Remote Sensing*, 52(3), pp. 1834-1842. https://doi.org/10.1109/TGRS.2013.2255614
- 8. Long, D.G., Brodzik, M.J. and Hardman, M.A., 2019. Enhanced-Resolution SMAP Brightness Temperature Image Products. *IEEE Transactions on Geoscience and Remote Sensing*, 57(7), pp. 4151-4163. https://doi.org/10.1109/TGRS.2018.2889427
- 9. Sethmann, R., Burns, B.A. and Heygster, G.C., 1994. Spatial Resolution Improvement of SSM/I Data with Image Restoration Techniques. *IEEE Transactions on Geoscience and Remote Sensing*, 32(6), pp. 1144-1151. https://doi.org/10.1109/36.338362
- Imaoka, K., Maeda, T., Kachi, M., Kasahara, M., Ito, N. and Nakagawa, K., 2012. Status of AMSR2 Instrument on GCOM-W1. In: SPIE, 2012. *Proceedings of SPIE*. Bellingham, USA: SPIE. Vol. 8528, Earth Observing Missions and Sensors: Development, Implementation, and Characterization II. Kyoto, Japan, 852815. https://doi.org/10.1117/12.977774
- 11. Wang, Y., Shi, J., Jiang, L., Du, J. and Tian, B., 2011. The Development of an Algorithm to Enhance and Match the Resolution of Satellite Measurements from AMSR-E. *Science China Earth Sciences*, 54(3), pp. 410-419. https://doi.org/10.1007/s11430-010-4074-0
- Maeda, T., Tomii, N., Seki, M., Sekiya, K., Taniguchi, Y. and Shibata, A., 2021. Validation of Hi-Resolution Sea Surface Temperature Algorithm toward the Satellite-Borne Microwave Radiometer AMSR3 Mission. *IEEE Geoscience and Remote Sensing Letters*, 19, 4500305. https://doi.org/10.1109/LGRS.2021.3066534
- Nunziata, F., Alparone, M., Camps, A., Park, H., Zurita, A.M., Estatico, C. and Migliaccio, M., 2021. An Enhanced Resolution Brightness Temperature Product for Future Conical Scanning Microwave Radiometers. *IEEE Transactions on Geoscience and Remote Sensing*, 60, 5301812. https://doi.org/10.1109/TGRS.2021.3109376

- Choi, M. and Hur, Y., 2012. A Microwave-Optical/Infrared Disaggregation for Improving Spatial Representation of Soil Moisture Using AMSR-E and MODIS Products. *Remote Sensing of Environment*, 124, pp. 259-269. https://doi.org/10.1016/j.rse.2012.05.009
- Santi, E., 2010. An Application of the SFIM Technique to Enhance the Spatial Resolution of Spaceborne Microwave Radiometers. *International Journal of Remote Sensing*, 31(9), pp. 2419-2428. https://doi.org/10.1080/01431160903005725
- Long, D.G., Hardin, P.J. and Whiting, P.T., 1993. Resolution Enhancement of Spaceborne Scatterometer Data. *IEEE Transactions on Geoscience and Remote Sensing*, 31(3), pp. 700-715. https://doi.org/10.1109/36.225536
- Hu, W., Yao, Z., Chen, S., Xu, Z., Liu, Y., Feng, Z. and Lightart, L., 2022. Spatial Resolution and Data Integrity Enhancement of Microwave Radiometer Measurements Using Total Variation Deconvolution and Bilateral Fusion Technique. *Remote Sensing*, 14(14), 3502. https://doi.org/10.3390/rs14143502
- Li, Y., Hu, W., Chen, S., Zhang, W., Guo, R., He, J. and Lightart L., 2019. Spatial Resolution Matching of Microwave Radiometer Data with Convolutional Neural Network. *Remote Sensing*, 11(20), 2432. https://doi.org/10.3390/rs11202432
- Liu, J.G., 2000. Smoothing Filter-Based Intensity Modulation: A Spectral Preserve Image Fusion Technique for Improving Spatial Details. *International Journal of Remote Sensing*, 21(18), pp. 3461-3472. https://doi.org/10.1080/014311600750037499
- Santi, E., Brogioni, M., Macelloni, G., Paloscia, S., Pampaloni, P. and Pettinato, S., 2008.
   A Simple Technique to Improve the AMSR-E Spatial Resolution at C-Band. In: IEEE, 2008. 2008.

   Microwave Radiometry and Remote Sensing of the Environment. Florence, Italy, pp. 1-4. https://doi.org/10.1109/MICRAD.2008.4579458
- 21. Meissner, T. and Wentz, F.J., 2012. The Emissivity of the Ocean Surface between 6 and 90 GHz over a Large Range of Wind Speeds and Earth Incidence Angles. *IEEE Transactions on Geoscience and Remote Sensing*, 50(8), pp. 3004-3026. https://doi.org/10.1109/TGRS.2011.2179662
- 22. Matrosov, S.Yu. and Shulgina, E.M., 1981. Scattering and Attenuation of Microwave Radiation by Precipitation. *Trudy Glavnoi Goefizicheskoi Observatorii im. A.I. Voeikova*, 448, pp. 85-94 (in Russian).
- Svendsen, E., Matzler, C. and Grenfell, T.C., 1987. A Model for Retrieving Total Sea Ice Concentration from a Spaceborne Dual-Polarized Passive Microwave Instrument Operating near 90 GHz. *International Journal of Remote Sensing*, 8(10), pp. 1479-1487. https://doi.org/10.1080/01431168708954790
- 24. Zabolotskikh, E.V. and Chapron, B., 2024. Estimation of Atmospheric Microwave Radiation Parameters over the Arctic Sea Ice from the AMSR2 Data. *IEEE Transactions on Geoscience and Remote Sensing*, 62, 4104211. https://doi.org/10.1109/TGRS.2024.3392369
- Ulaby, F.T., Moore, R.K. and Fung, A.K., 1981. Microwave Remote Sensing: Active and Passive. Volume 1. Microwave Remote Sensing Fundamentals and Radiometry. Reading, MA: Addison-Wesley Publishing Co., 456 p.
- 26. Zabolotskikh, E. and Azarov, S., 2022. Wintertime Emissivities of the Arctic Sea Ice Types at the AMSR2 Frequencies. *Remote Sensing*, 14(23), 5927. https://doi.org/10.3390/rs14235927
- 27. Zabolotskikh, E.V., Balashova, E.A. and Chapron B., 2019. Advanced Method for Sea Ice Concentration Retrieval from Satellite Microwave Radiometer Measurements at Frequencies near 90 GHz. *Sovremenniye Problemy Distantsionnogo Zondirovaniya Zemli iz Kosmosa*, 16(4), pp. 233-243. https://doi.org/10.21046/2070-7401-2019-16-4-233-243 (in Russian).

28. Zabolotskikh, E.V., Zhivotovskaia, M.A., Lvova, E.V. and Yarusov, K.I., 2024. Arctic Sea Ice Classification Using AMSR2 Data. *Sovremenniye Problemy Distantsionnogo Zondirovaniya Zemli iz Kosmosa*, 21(5), pp. 263-274. https://doi.org/10.21046/2070-7401-2024-21-5-263-274 (in Russian).

Submitted 05.03.2025; approved after review 20.04.2025; accepted for publication 11.07.2025.

About the authors:

Elizaveta V. Zabolotskikh, Leading Research Associate, Laboratory of Satellite Oceanography, Russian State Hydrometeorological University (98 Malookhtinsky Ave., Saint Petersburg, 195196, Russian Federation), DSc. (Phys.-Math.), ORCID ID: 0000-0003-4500-776X, ResearcherID: R-2221-2016, Scopus Author ID: 6506482460, liza@rshu.ru

Bertrand Chapron, Head of Satellite Oceanography Department, Institut Français de Recherche pour l'Exploitation de la Mer, Ifremer, (Centre de Bretagne, ZI Pointe du Diable CS 10070, Plouzané, 29280, France), DSc. (Phys.-Math.), ORCID ID: 0000-0001-6088-8775, Scopus Author ID: 56209544000, bertrand.chapron@ifremer.fr

Contribution of the co-authors:

**Elizaveta V. Zabolotskikh** – methodology, numerical simulations, satellite data processing, data analysis, text writing

Bertrand Chapron - consulting on method development, participation in the analysis of results

The authors have read and approved the final manuscript. The authors declare that they have no conflict of interest.